Modelling of the kinetics of pitting corrosion by metal dusting

Aurélien Fabas, Daniel Monceau, Sébastien Doublet, Aurélie Vande Put

Modelling of the kinetics of pitting corrosion by metal dusting

Aurélien Fabas [a], Daniel Monceau [a,*], Sébastien Doublet [b], Aurélie Rouaix-Vande Put [a]

[a] Université de Toulouse, Institut Carnot CIRIMAT, INPT-ENSIACET, 4 allée Emile Monso, BP-44362, 31432 Toulouse Cedex 4, France
[b] Air Liquide R&D, Paris-Saclay Research Center, 1 chemin de la porte des loges, BP-126, 78354 Jouy-en-Josas Cedex, France

ARTICLE INFO

Keywords:
A. Stainless Steel
B. Modelling studies
C. High temperature corrosion
C. Pitting corrosion

ABSTRACT

Commercial 800HT alloy was exposed to 49.1%H_2–12.8%CO–3.1%CO_2–1.6 CH_4–33.4%H_2O gas at 21 bars and 570 °C up to 5000 h. Metal dusting attack by pitting was observed. The kinetics parameters were identified to be the incubation time, pit density and individual pit growth rate. These parameters were introduced in a nucleation-growth model to simulate the pitted surface area kinetics. This model was then extended to the volume considering several geometrical hypotheses. Considering only surface coalescence of the pits without their volume coalescence allowed to correctly reproduce the experimental mass loss kinetics. An even simpler conservative model was proposed for an easy lifetime modelling.

1. Introduction

When Ni-, Fe- or Co-based alloys are exposed to highly carburising atmospheres ($a_C > 1$), a catastrophic corrosion may take place [1,2]. This phenomenon, called "metal dusting", happens at a temperature in the range of 400–800 °C. It is characterised by the disintegration of the alloy into a dust of fine metallic particles and graphitic carbon, named "coke". Mechanisms have been proposed to explain metal dusting attack of Fe-based [1,3,4,6] and of Ni-based alloys [5,7]. Metal dusting is a very complex type of corrosion which depends on the nature of the alloy [8,9], its microstructure [10,11] and composition [12,13]. Of course, it is also greatly influenced by the atmosphere composition [3,8,14], the temperature [15,16] and the overall pressure [17,18]. Due to the low oxygen partial pressure (below 10^{-20} bar), only very stable oxides such as chromia, alumina, silica or some spinels can form. Chromia and alumina are well known for limiting or preventing carbon ingress into the alloy. In this case, the fast degradation due to metal dusting occurs after an incubation time, which duration depends on the quality and stability of the protective oxide scale. An alloy which can form such an oxide scale will be corroded when the scale fails to protect the material, due to cracks, spalls or other defects. The alloy will be degraded locally, via a pitting-type mechanism [4,8,9,19]. Even if pitting is always noticed, only few studies focus on this phenomenon [19–23]. Moreover, as far as the authors know, the kinetics of metal dusting by pitting has never been modelled, despite existing modelling efforts in other type of pitting corrosion in aqueous environments [24]. The present work aims to propose a simple kinetic model for pitting-type metal dusting corrosion, which could be used to quantify the degradation. It is based on simple optical surface observations on 800HT commercial alloy. The mass change is also assessed using a study of pit morphology characterised on cross sections. The limits of the model and the physical phenomenon from which pitting kinetics is evaluated are discussed.

2. Materials and experiments

The chemical composition of the 800HT alloy studied in the present work was obtained by EDS. Its composition is presented in Table 1. The 800HT samples were cut in a commercial rod to obtain disc specimens with a diameter and a thickness of approximately 14 mm and 1.6 mm respectively. A hole was drilled at the centre of each specimen. These samples were held by alumina sticks in the subsequent exposure test. One side of the sample faces the sample holder – called "internal side" below: the other side faces the inner surface of the furnace – called "external side" below. The specimens were chamfered to limit edge effects. Samples were mechanically ground to a P600 grit finish, and ultrasonically cleaned in acetone and in ethanol, and dried before the experiment.

The isothermal corrosion test was performed in a vertical furnace. Three 800HT samples were exposed simultaneously to a 49.1%H_2–12.8%CO–3.1%CO_2–1.6%CH_4–33.4%H_2O gas mixture at 570 °C and 21 bars. This gas mixture was obtained by first creating a mixture of H_2, CO, CO_2 and CH_4 using pure pressurised gases and

* Corresponding author at: CIRIMAT UMR5085 CNRS-INPT-UPS, ENSIACET, 4, allée Emile Monso, BP-44362, 31030 Toulouse Cedex 4, France. Tel.: +33 5 34 32 34 22; fax: +33 5 34 32 34 22.
E-mail address: daniel.monceau@ensiacet.fr (D. Monceau).

http://dx.doi.org/10.1016/j.corsci.2015.05.061

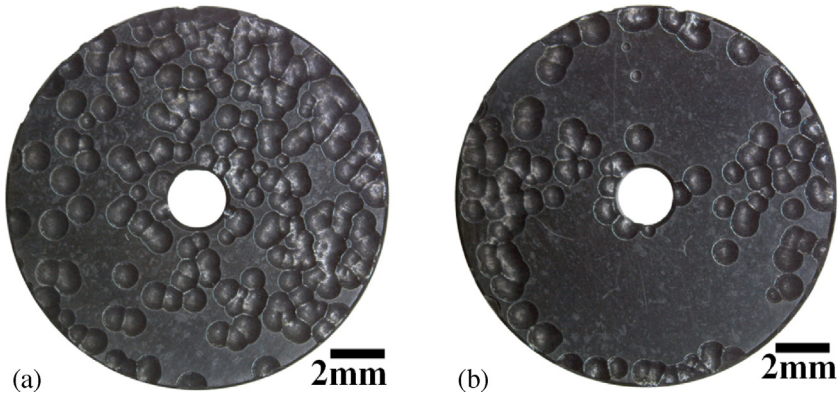

Fig. 1. Pictures of (a) external and (b) internal side of 800HT sample #3 after 4941 h in H_2–CO–CO_2–CH_4–H_2O at 570 °C, 21 bar.

mass flow controllers on each line for the setting of the dry gas composition. Then, the water was introduced in the preheated gas via a calibrated High Pressure Liquid Chromatography (HPLC) pump. The homogenisation of the gas composition and temperature was promoted by flowing the atmosphere through a ceramic foam at the furnace inlet. The total system pressure was controlled downstream of the furnace via a backpressure regulator placed on the outlet dry gas line. The amount of water was controlled by weighting the condensed water at the equipment outlet. The linear gas flow rate was adjusted to 0.28 cm/s and 2290 scc/h/sample. In the aforementioned atmosphere, the carbon activity a_c, calculated from the synthesis gas reaction, and the partial pressure of oxygen P_{O2}, calculated from the water decomposition reaction, were 32.0 and 7.1×10^{-26} bar respectively, using thermodynamical data from Ref. [25].

The three 800HT samples were removed approximately every 500 h. After being cleaned ultrasonically in ethanol and being dried, they were weighted on a Sartorius CPA225DOCE balance with a precision of 0.01 mg. Pictures (with a precision of 7 μm/pixel) of each sample were also taken on both faces thanks to a Zeiss Stemi 2000-C Stereomicroscope, and further analysed with ImageJ software. The entire surface was analysed except a 1 mm thick hoop, which was systematically removed from the sample edges. This was done in order to limit any edge effect in the surface analysis. It was done for the external edge of the sample as well as for the internal edge, i.e. around the central hole. Pit diameter was averaged by measurements on numerous pits. The averaged, maximum and minimum incubation times were determined by extrapolating backwards (to zero size) the experimental kinetics of pit diameter growth.

After the exposure test, each sample was characterised by X-ray diffraction (XRD) on a Seifert 3000TT apparatus with a copper anti-cathode (λ = 1.54056 Å). XRD were carried out using a small incidence angle of 2°. Optical microscopy, Raman spectroscopy and scanning electron microscopy (SEM) were performed on one side and on cross section for each sample. The optical microscope used in this study was a Nikon Eclipse MA200. Raman spectroscopy was done using a Labram HR 800 Yvon Jobin spectrometer equipped with a confocal microscope (magnifications are 10×, 50× and 100×) using a 514 nm argon ion laser. SEM observations were carried out using a LEO 435 VP using secondary (SE) and backscattered electrons (BSE) modes. EDS analyses were done using an IMIX system from PGT. Cr-carbides were revealed by etching in Murakami reagent (1 g $K_3Fe(CN)_6$, 1 g KOH, 10 mL H_2O) at room temperature during 30 s.

Table 1
Chemical composition of the 800HT alloy used in this study, measured by EDS.

Element	Fe	Ni	Cr	Ti	Al	Si	Mn	Cu
%at	Bal.	28.0	22.0	0.8	1.5	1.2	0.8	0.2

3. Results

3.1. Overview

The global behaviour was found to be the same for all samples. Pitting was first detected after 1147 h of exposure (second removal) on both sides. The external face was the most severely attacked for all specimens. The pits had a circular shape and were not randomly distributed as it can be seen in Fig. 1. Relevant weight mass loss occurred also after 1147 h (Fig. 2). The oxide scale was mainly constituted of Cr_2O_3. $(Fe,Cr)_3O_4$ spinel oxide, $(Cr,Fe)_{23}C_6$ carbides and amorphous and crystallised carbon were also detected by XRD and Raman spectroscopy (Fig. 3). Among the numerous areas analysed by Raman spectroscopy, no change on the composition of chromia, spinel oxide or of the proportion of each oxide was noticed. Only carbon proportion was observed to vary.

3.2. Mass change

No significant mass change occurred before 1147 h of exposure (Fig. 2). Sample #1, definitively removed after 1987 h of exposure, was characterised by a shorter incubation time than samples #2 and #3, definitely removed after 3472 h and 4941 h, respectively. Samples #2 and #3 presented the same incubation time and an almost linear mass loss kinetics after 2322 h and 3472 h, respectively. This

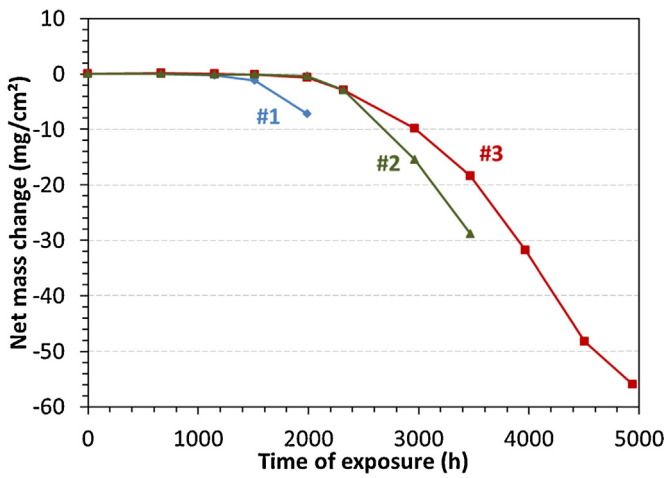

Fig. 2. Net mass change of the 800HT samples in H_2–CO–CO_2–CH_4–H_2O at 570 °C, 21 bar.

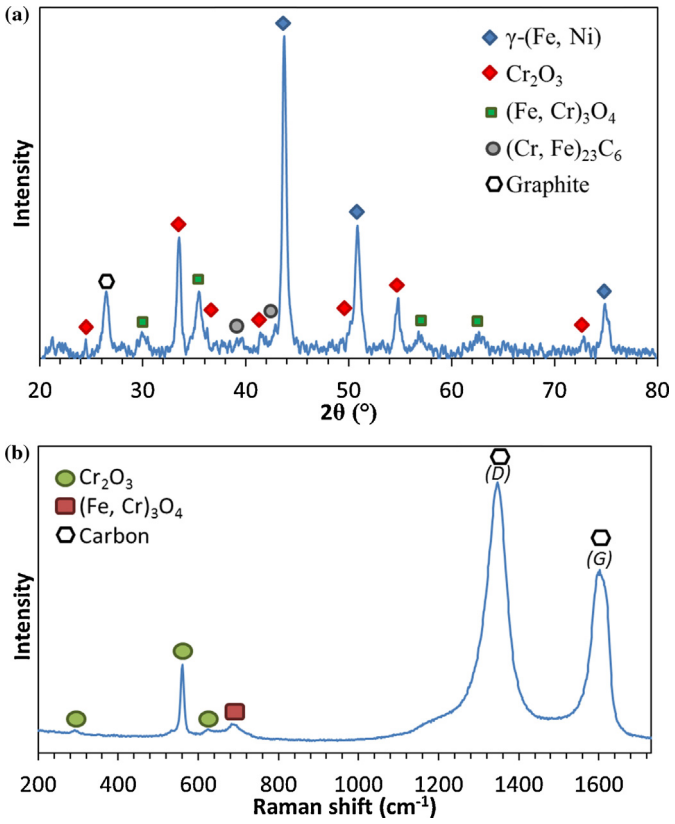

Fig. 3. (a) XRD and (b) Raman spectra of 800HT sample #1 after 1987 h in H_2–CO–CO_2–CH_4–H_2O at 570 °C, 21 bar. (D) and (G) represent signals for disordered and ordered carbon, respectively.

linear kinetics for the mass loss corresponded to an average rate of -0.026 ± 0.01 mg/cm^2/h for both samples.

3.3. Pitting characterisation

Corrosion by pitting can be characterised by multiple parameters. The first one is the time needed to see the first pits at the surface of a corroded material. This first parameter is called the incubation time for pitting. The second parameter is the density of pits per unit area. This quantifies the global attack of the sample. But it is also interesting to follow a third key parameter, which is the individual pit growth rate. This is done to link a physical model of degradation at the local scale with the overall degradation kinetics. The last key parameter is the morphology of pit. Indeed, even a large number of pits with a high growth rate can lead to a slow

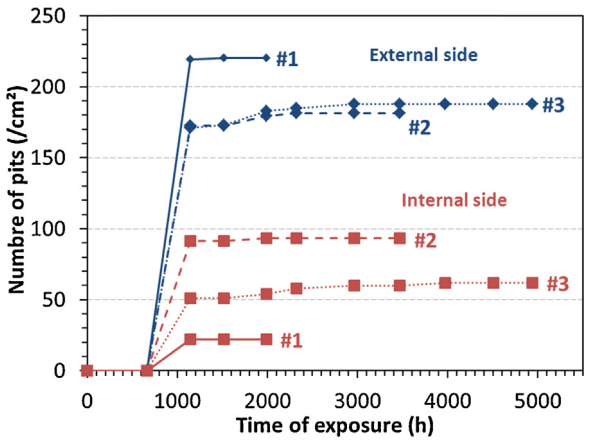

Fig. 5. Evolution of the number of pits on external (blue diamonds) and internal (red squares) side of 800HT samples #1 (continuous line), #2 (dashed line) and #3 (dotted line) in H_2–CO–CO_2–CH_4–H_2O at 570 °C, 21 bar. (For interpretation of the references to color in this figure legend, the reader is referred to the web version of this article.)

degradation if the pits do not grow inward into the corroded material. This is necessary to link the surface area of attack with the observed mass loss.

The main symbols and units used through the article are defined in Appendix.

3.3.1. Surface

The pits contained a porous mixture of corrosion products due to the metal dusting attack, as illustrated in Fig. 4. Pit corrosion products (noted A in Fig. 4) were composed of Cr-depleted austenitic particles (brightest contrast), Fe–Cr spinels (grey particles), graphite and carbon-rich particles (darkest contrast). The composition of the oxide scale at the edges of the pits (noted B in Fig. 4) was not modified by the latter. For the three samples, the pit density was larger on the external side than on the internal side (Fig. 5).

Pit growth has been studied on both sides of the three samples, tracking pit diameter evolution (Fig. 6). For samples #2 and #3 (internal side), pits had initially an irregular shape before getting circular, as already notice by Zeng et al. on 9Cr–1Mo steel [6]. This could explain the plateau at the beginning of the pit growth, visible in Fig. 6d–f. Note that this plateau, corresponding to a pit size of about 0.1 mm, was not taken into account for the estimation of the incubation period and for the calculation of the growth rate. If the pit shape at the sample surface is considered close to the one of a disc, the lateral pit growth kinetics is linear and does not depend on the incubation duration. It is characterised by a lateral

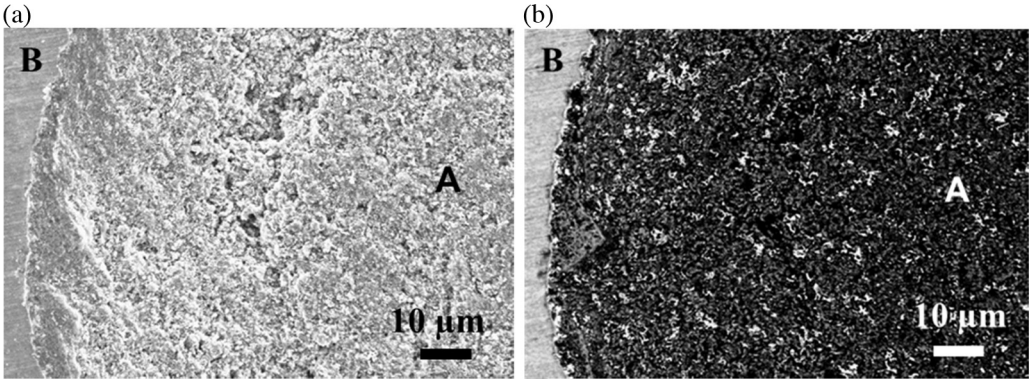

Fig. 4. (a) SE and (b) BSE SEM pictures of a pit containing corrosion products (noted A) and the oxide scale at it edges (noted B) after 1987 h in H_2–CO–CO_2–CH_4–H_2O at 570 °C, 21 bar.

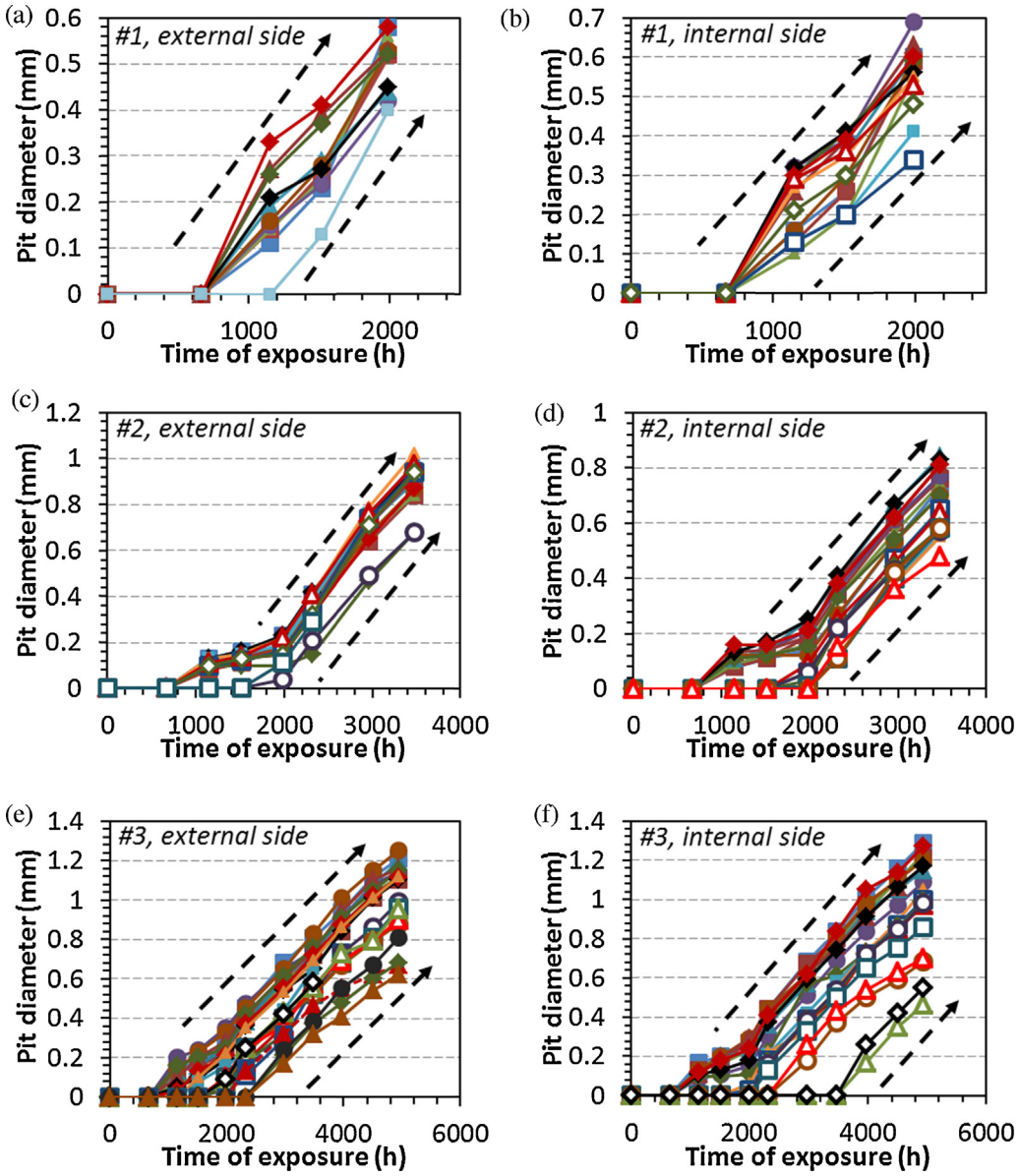

Fig. 6. Pit diameter growth of internal and external sides of 800HT samples (a and b) #1, (c and d) #2 and (e and f) #3.

pit growth rate constant k_d. The diameter of the pit, d, can then be expressed as:

$$d(t, t_0) = k_d(t - t_0) \quad (1)$$

with t the time, t_0 the incubation time of the pit and k_d the lateral pit growth rate constant, calculated using the slope of the pit diameter evolution versus the exposure time.

The lateral pit growth rate constant (k_d) measurement is less precise for sample #1 than for samples #2 and #3 due to the shorter exposure time. Data are gathered together in Table 2. The incubation time t_0 of the pitting phenomenon was obtained applying the lateral pit growth rate constant k_d to all pits. The averaged, minimum and maximum values of the obtained incubation times are listed in Table 3. It shows that the internal sides were less attacked than the external sides, but that the pit diameter growth kinetics were similar, Table 2. Moreover, there is almost no influence of the sample side on the incubation time, Table 3. The evolution of the pitted surface area fraction versus time is characterised by an S shape curve for sample #3, Fig. 7. The pitted surface area fraction of samples #1 and #2 seems to follow the same evolution but their exposure duration was not long enough to confirm this tendency, Fig. 7.

Table 2
Pit density after 1000 h and pit diameter growth rate constant of the 3 specimens 800HT.

Sample	Side	Lateral pit growth rate constant (μm/h)	Pit density/cm^2 at 1000 h
#1	External	0.38	219.4
	Internal	0.40	22.0
#2	External	0.32	171.1
	Internal	0.28	51.1
#3	External	0.46	172.5
	Internal	0.40	91.6
Average	External	0.38	187.7
	Internal	0.36	54.9

Table 3
Average, minimum and maximum incubation times of both sides of the 3 specimens of 800HT.

Sample	Side	Average incubation time (t_0) (h)	Minimum incubation time, $t_{0_{min}}$ (h)	Maximum incubation time, $t_{0_{max}}$ (h)
#1	External	600	50	1000
	Internal	600	50	1000
#2	External	1200	800	1400
	Internal	800	700	1000
#3	External	1600	1400	1800
	Internal	1500	1300	1700
Average	External	1100	800	1400
	Internal	1000	700	1200

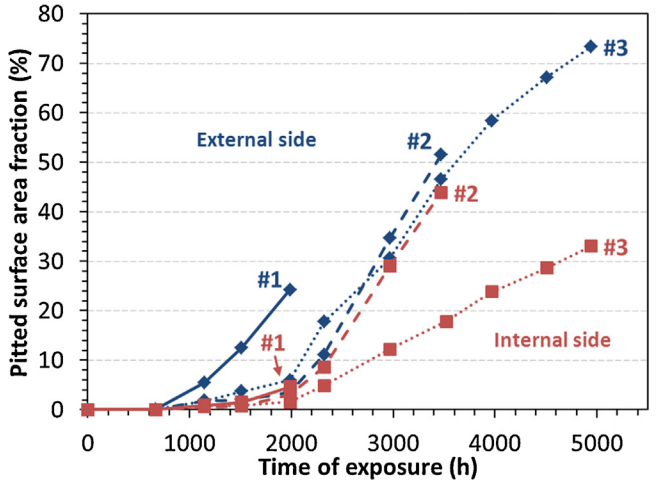

Fig. 7. Evolution of the pitted surface area fraction for external (blue diamond) and internal (red squares) sides of 800HT samples #1 (continuous line), #2 (dashed line) and #3 (dotted line) in H_2–CO–CO_2–CH_4–H_2O at 570 °C, 21 bar. (For interpretation of the references to color in this figure legend, the reader is referred to the web version of this article.)

3.3.2. Volume

The cross sections of the 3 samples show a circular-segment shape for isolated pits (shown for sample #1 in Fig. 8a). The pit depth/diameter ratio F was calculated for all isolated pits on both sides of each sample. It was found that the pit depth, p, is about the fifth of the pit diameter:

$$F = \frac{p}{d} \tag{2}$$

with F equal to 0.19 ± 0.03, 0.20 ± 0.03 and 0.20 ± 0.06 for sample #1, #2 and #3, respectively. A value of 0.2 will be used later in this article.

An oxide, identified as $(Fe,Cr)_3O_4$ by Raman spectroscopy, was observed at the pit/alloy interface (shown for sample #1 in Fig. 9a). SEM observations showed remains of an internal oxidation layer

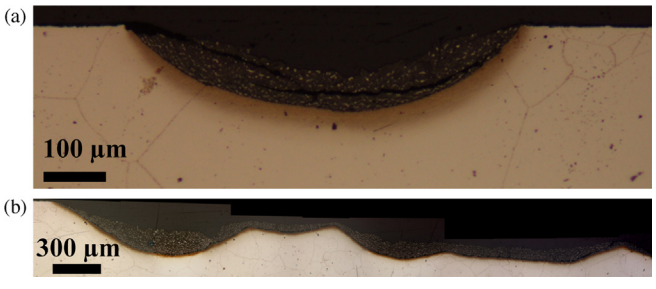

Fig. 8. (a) Cross section of etched sample #1 after 1987 h of exposure in H_2–CO–CO_2–CH_4–H_2O at 570 °C, 21 bar. (b) Overlapping between pits after 4941 h for sample #3.

up to 2 µm thick along the entire pit/alloy interface for the 3 samples. Below the internal oxidation zone, along the circumference of the pit, a carburised zone is visible for all the samples (shown for sample #1 in Fig. 9b). This layer is about 15 µm thick, whatever the sample is and despite different exposure times. EDS analysis showed no variation on the proportion of metallic elements in the alloy between the carburised zone and the bulk. No Cr depletion was evidenced in this area. Above the oxide layer, metal dusting corrosion products in the pit are organised as layered microstructure of Cr- and Fe-depleted alloy, carbon-rich particles and Fe–Cr oxide. Some coalescence of pits was observed. The more the pits overlapped, the more their bottom flattened, leading eventually to a cylinder shape (Fig. 8b).

4. Kinetics modelling of the pitting

4.1. Surface

4.1.1. Theory

The most common statistical model to describe the nucleation and growth phase transformation kinetics is the Johnson–Mehl–Avrami–Kolmogorov (JMAK) phenomenological model [26–30]. This model has been used for 70 years due to its simplicity that resides in its formula:

$$V(t) = 1 - e^{-V_e(t)} \tag{3}$$

where V is the volume fraction of transformed phase and $V_e(t)$ the volume fraction of transformed phase considering no overlap between the growing nuclei.

If the studied phenomenon appears at a time $t_0 > t = 0$, the time shift can be injected using $(t - t_0)$ instead of t. This law depends only on the number of nuclei by volume unit $N_V(t,t_0)$ and of the volume of a nucleus $V_N(t,t_0)$. This law can then be rewritten as follows:

$$V(t, t_0) = 1 - e^{-N_V(t,t_0)V_N(t,t_0)} \tag{4}$$

The main limitation of this model resides in the main hypotheses that nucleation and growth are isotropic. These hypotheses imply that this model cannot be applied to the particular case where nucleation happens at the surface of a material. This issue was solved separately by Johnson and Mehl [30] and Mampel [31]. They considered nucleation at the surface with an isotropic or quasi-isotropic growth. The studied volume was then cut in slices of a thickness dx and the transformed surface area fraction could then be described as:

$$\theta(x, t, t_0) = 1 - e^{-N(x,t,t_0)A(x,t,t_0)} \tag{5}$$

with $\theta(x,t,t_0)$ the transformed surface area fraction at the thickness x, $N(x,t,t_0)$ and $A(x,t,t_0)$ the number of nuclei per unit area and their area, respectively. The authors can then deduce the volume from summing all the slices. Due to the complicated calculations leading to a numerical solution for this model, associated to the complexity added by the non-isotropic pit growth in the metal dusting experiment ($F = 0.2$), this model was not used in the present study. Instead,

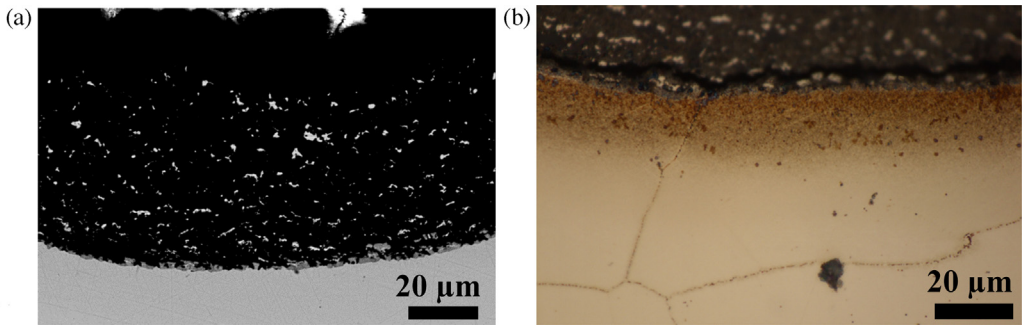

Fig. 9. (a) BSE SEM and (b) optical (after etching) cross section pictures of the bottom of a pit of sample #1 after 1987 h of exposure in H_2–CO–CO_2–CH_4–H_2O at 570 °C, 21 bar.

a simpler model was looked for, using some approximations which can be done for the particular case of metal dusting. Evans [32] proved mathematically that the surface fraction covered by films spreading out as expanding circles that have nucleated randomly on the studied area follows a particular case of JMAK kinetics:

$$\theta(t, t_0) = 1 - e^{-N(t,t_0)A(t,t_0)} \tag{6}$$

It has to be noted that Evans' formula is the same as the one used by Mampel and Johnson and Mehl at the surface of the system (i.e. for $x = 0$). This simple model has already proven its usefulness in modelling breakaway oxidation kinetics of FeNiCr alloys [33].

4.1.2. Application to the current study

As it was noticed previously, the number of pits per unit area observed in the present study does not depend on time. Nucleation can then be considered as instantaneous, and the number of pits per unit area, N_p, can be expressed as follows:

$$N_p(t, t_0) = \begin{cases} 0 & \text{for } t < t_0 \\ N_0 & \text{for } t \geq t_0 \end{cases} \tag{7}$$

where N_0 is the number of pits per unit area nucleating at the time t_0.

The present study revealed that the pit diameter growth kinetics was linear. The surface area of a single pit, A_p, can then be expressed as:

$$A_p(t, t_0) = \pi \left(\frac{k_d}{2}\right)^2 (t - t_0)^2 \tag{8}$$

The Eqs. (7) and (8) can then be injected in Evans' formula (Eq. (6)) for $t \geq t_0$:

$$\theta(t, t_0) = 1 - e^{-\pi N_0 \left(\frac{k_d}{2}\right)^2 (t-t_0)^2} \tag{9}$$

This pitted surface area fraction has to be understood as the ratio of the pitted area divided by the studied area.

This model of metal dusting pitting kinetics makes use of the following hypotheses which can be discussed with regard to the experimental results. First, it was considered that all the nuclei appeared at time t_0 on the surface. This was supported by our observations. The second hypothesis of the model is that pits are circular and grow following a linear kinetics, characterised by the lateral pit growth rate constant k_d. This was also observed experimentally and the corresponding values were given in Table 2. The third hypothesis is that the nuclei are randomly distributed all over the surface. As shown on the pictures of the surface (Fig. 1), this is not true in our case as edges were more attacked. This would be a source of error for the predictions made by the model. Considering our objective to find a model which represents the material behaviour and not the effect of the sample shape, the surface close to the edges was not considered for image analysis.

This model was then applied to both sides of the 3 samples and the results are shown in Fig. 10. Whereas the model fits well with the experimental data obtained with the sample #2, the calculated pitted surface area fraction increases more rapidly than the experimental one for samples #1 and #3. To better fit the experimental data for the three samples, a new parameter was introduced in Eq. (9). This parameter takes into account the possibility that a part of the surface is not affected by metal dusting pitting during the time of the experiment, as this can be observed on the samples:

$$P(t, t_0) = B \cdot \theta(t, t_0) = B \left(1 - e^{-\pi N_0 \left(\frac{k_d}{2}\right)^2 (t-t_0)^2}\right) \tag{10}$$

The parameter B can be considered as a fit parameter and chosen to obtain the best fit for both sides of specimens #1 and #3. It can be concluded that for each side of both samples 85% of the surface was sensitive to metal dusting corrosion (Fig. 11). The applicability of Evans' model to the 3 samples indicates that the hypothesis of random pitting is satisfactory when applied to the reactive area, i.e. 85–100% of the surface, depending on samples.

To summarise, it was shown that the pitting-corrosion kinetics can be modelled by determining the number of pits per unit area N_0 and the lateral pit growth rate constant k_d. The fit parameter B takes into account the possibility that a part of exposed area is immune to pitting. The incubation time t_0 is a shifting parameter allowing to apply the model even if pitting does not occur immediately.

4.2. Volume kinetics

It is interesting to model the volume kinetics of the pitting for the following reason. A common technique to determine experimentally the metal dusting attack is the measurement of mass change after sample cleaning. It is obviously related to the pit volume. It is easy to show that the mass increase due to oxidation and carbon dissolution in the alloy is negligible compared to the mass loss due to metal dusting. As structural materials subjected to metal dusting have to sustain mechanical stresses in service, it is useful to link the surface area of attack to the depth of the attack for a vessel under pressure. The evaluation of the material mass loss can be modelled considering some hypotheses. As seen previously, experimental work showed that pit depth was proportional to pit diameter. If we assume that this relationship is always verified, combining Eqs. (1) and (2) leads to express the pit depth as:

$$p(t, t_0) = F \cdot d(t, t_0) = F \cdot k_d(t - t_0) \tag{11}$$

with $d(t,t_0)$ the diameter of the pit and F the pit depth/diameter ratio ($F = 0.2$).

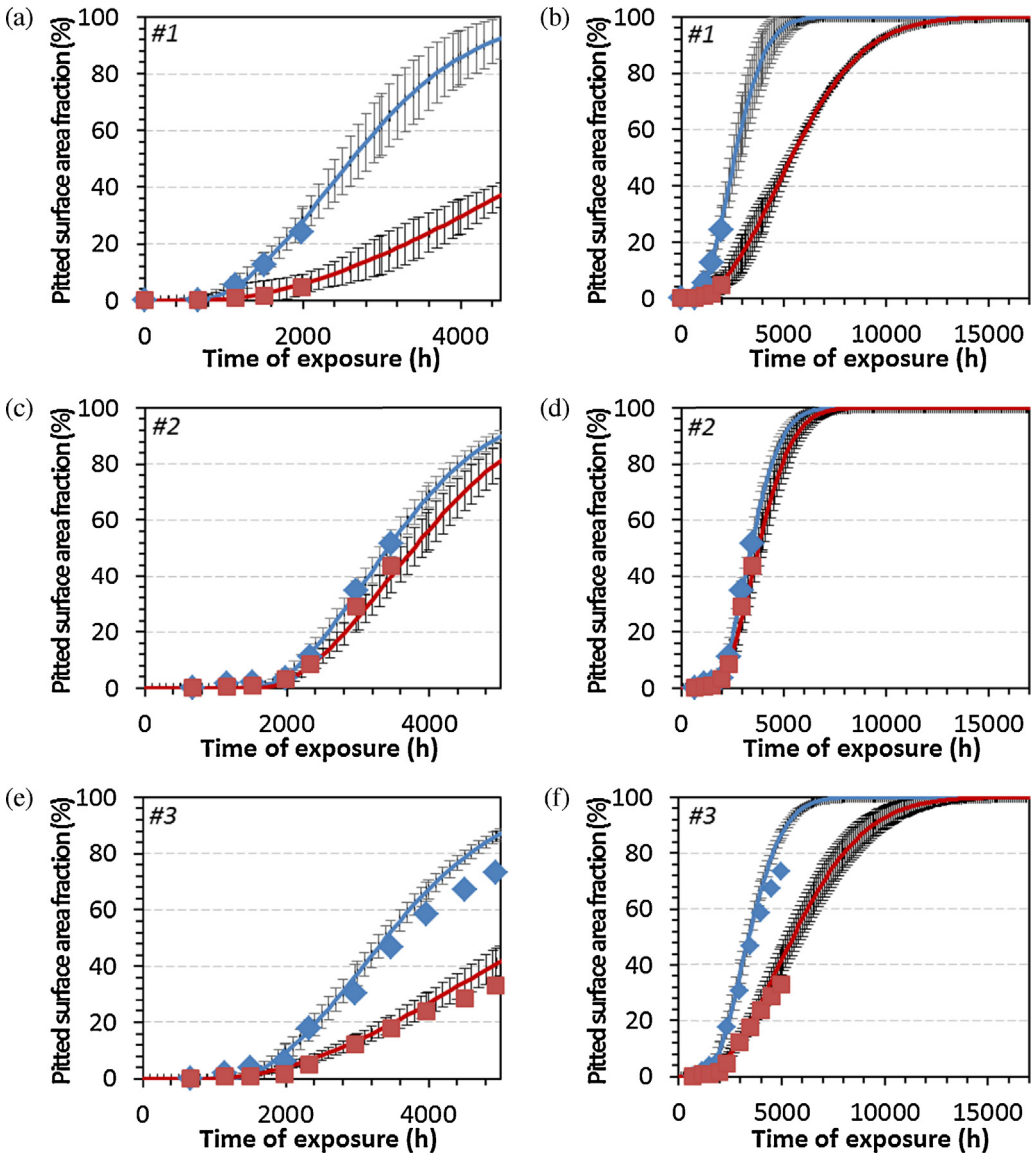

Fig. 10. Experimental (symbols) and calculated (curves) pitted surface area fraction after 5000 h and 17000 h in H_2–CO–CO_2–CH_4–H_2O at 570 °C, 21 bar for external (blue diamonds) and external (red squares) side of (a and b) sample #1, (c and d) sample #2, and (e and f) sample #3 for a maximum pitted surface area fraction equal to 1. (For interpretation of the references to color in this figure legend, the reader is referred to the web version of this article.)

To determine the pit volume, it is necessary to know the relationship between its surface area and its volume. The pits observed on the sample surface and on the cross sections have a circular shape. Assuming that this is always the case the pit volume, $V_p(t,t_0)$, can be expressed as the volume of a spherical cap:

$$V_p(t,t_0) = \frac{\pi p(t,t_0)}{6}\left[3\left(\frac{d(t,t_0)}{2}\right)^2 + p(t,t_0)^2\right] \quad (12)$$

The volume to surface area ratio can then be calculated using Eqs. (8) and (12):

$$\frac{V_p(t,t_0)}{A_p(t,t_0)} = p(t,t_0)\left[\frac{1}{2} + \frac{2}{3}\left(\frac{p(t,t_0)}{d(t,t_0)}\right)^2\right] \quad (13)$$

Injecting Eq. (11) in Eq. (13) allows simplifying:

$$\frac{V_p(t,t_0)}{A_p(t,t_0)} = S_f k_d (t - t_0) \quad (14)$$

with S_f the shape factor of the pit. The shape factor depends on the pit depth/diameter ratio F and the pit volume/cylinder volume ratio V_R.

$$S_f = F \cdot V_R \quad (15)$$

For a cylinder morphology, V_R is equal to 1, S_f is equal to F.

For a spherical-cap morphology, the spherical-cap/cylinder volume ratio V_R is:

$$V_R = \frac{V_p}{pA_p} = \frac{1}{2} + \frac{2}{3}F^2 \quad (16)$$

4.3. Models for pitting-corrosion kinetics

Several models can be used to calculate the total volume of all the pits, depending on the morphology of the pits. These geometrical models are summarised in Fig. 12. Several models are considered in order to reach different levels of approximation of the experimental data.

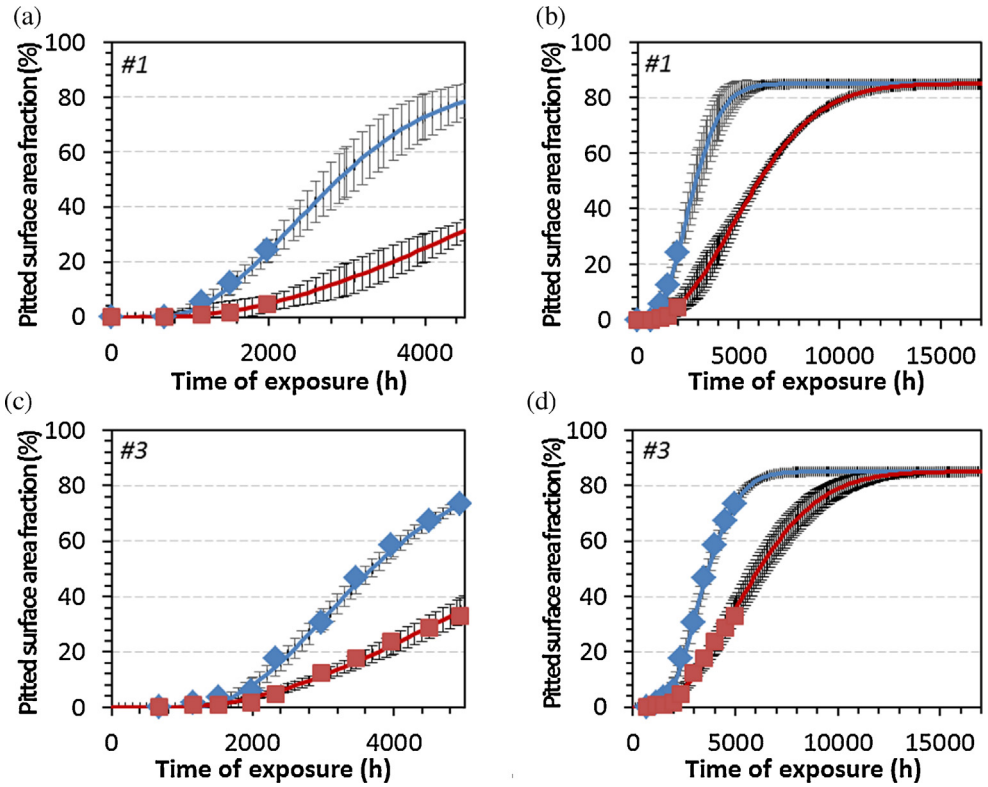

Fig. 11. Experimental (symbols) and calculated (curves) pitted fraction area after 5000 h and 17000 h in H_2–CO–CO_2–CH_4–H_2O at 570 °C, 21 bar for external (blue diamonds) and external (red squares) side of (a and b) sample #1, (c and d) sample #3, for a maximum pitted surface area fraction equal to 0.85. (For interpretation of the references to color in this figure legend, the reader is referred to the web version of this article.)

It is interesting to establish descriptive models to be as close as possible to the experimental data.

4.3.1. Model I: growth of N_0 *pits with a spherical-cap morphology*

As seen previously, pits are characterised by a spherical-cap morphology (Fig. 8a). It was also shown that the pitting phenomenon can be characterised by the instantaneous nucleation of N_0 pits per unit area at the time t_0. The simplest way to express the mass loss is to consider no coalescence of the pits at all (Model I in Fig. 12). The pitted surface area fraction, θ, can then be written as the sum of the surface of the N_0 pits per unit area:

$$\theta(t, t_0) = \sum_{i=1}^{N_0} \frac{A_{p_i}(t, t_0)}{S} \tag{17}$$

A_{p_i} is given by Eq. (8). Hence:

$$\theta(t, t_0) = \pi N_0 \left(\frac{k_d}{2}\right)^2 (t - t_0)^2 \tag{18}$$

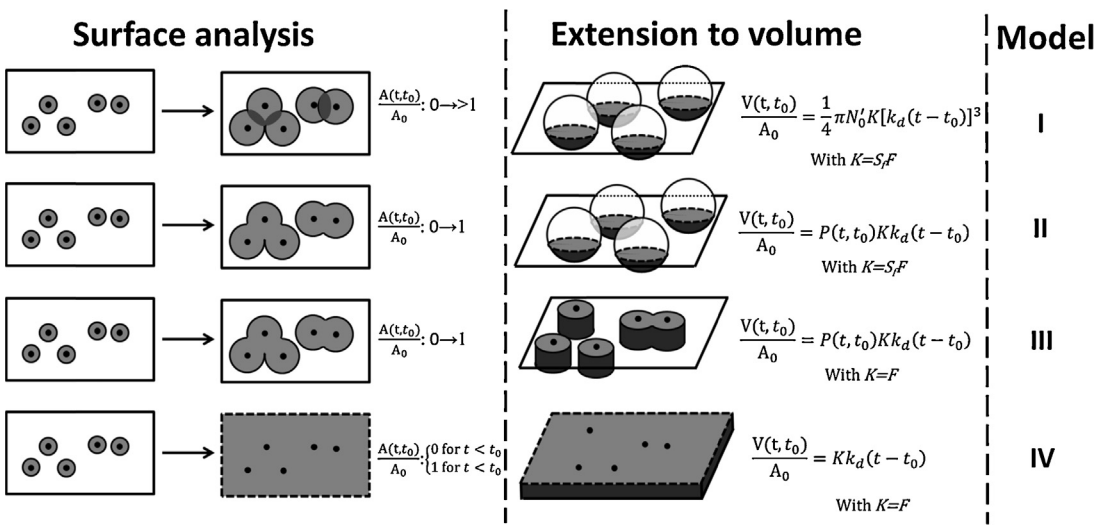

Fig. 12. Summary of the different kinetic models for surface pitting with their extensions to the volume.

Knowing the lateral pit growth rate constant k_d, the incubation time t_0, and the shape of the pit (Eq. (14)), the volume lost per unit area of the sample, V_L/S, can be expressed as:

$$\frac{V_L}{S}(t, t_0) = \theta(t, t_0) S_f k_d (t - t_0) = \frac{1}{4}\pi N_0 S_f [k_d (t - t_0)]^3 \quad (19)$$

To obtain the volume of all the pits per unit area, V_L^{tot}/S, both sides have to be considered since their pitting kinetics were observed to be different:

$$\frac{V_L^{tot}}{S}(t, t_0^{ext}, t_0^{int}) = \frac{1}{2}\left(\frac{V_L^{ext}}{S}(t, t_0^{ext}) + \frac{V_L^{int}}{S}(t, t_0^{int})\right) \quad (20)$$

with t_0^{ext} and t_0^{int} the incubation times on external and internal sides, respectively.

Injecting Eq. (19) in Eq. (20) for both sides of the sample:

$$\frac{V_L^{tot}}{S}(t, t_0^{ext}, t_0^{int}) = \frac{1}{8}\pi S_f \left[N_0^{ext} k_d^{ext3} (t - t_0^{ext})^3 + N_0^{int} k_d^{int3} (t - t_0^{int})^3\right] \quad (21)$$

It is then easily possible to express the overall mass change per unit area $\Delta m/S$:

$$\frac{\Delta m}{S}(t, t_0^{ext}, t_0^{int}) = -\rho_{all} \frac{V_L^{tot}}{S}(t, t_0^{ext}, t_0^{int}) \quad (22)$$

with ρ_{all} the alloy density.

Using Eq. (21), Eq. (22) can be also expressed as follows:

$$\frac{\Delta m}{S}(t, t_0^{ext}, t_0^{int}) = -\frac{1}{8}\rho_{all}\pi S_f \left[N_0^{ext}(k_d^{ext}(t - t_0^{ext}))^3 + N_0^{int}(k_d^{int}(t - t_0^{int}))^3\right] \quad (23)$$

Fig. 13 shows the comparison between this kinetic model and the experimental data. As expected, the agreement is correct only for short-time exposures, as long as the effect of coalescence is negligible.

4.3.2. Model II: surface coalescence of pits with a spherical-cap morphology

Taking into account the coalescence of pits in the three dimensions complexifies the mathematics. In order to take into account the surface coalescence of the pits without dealing with the mathematics of volume coalescence, the following model (Model II) is proposed. As pit coalescence happens, the pitted surface area increases slower than in the absence of coalescence (Model I) for the same number of pits N_0.

In the Model II (represented in Fig. 12), the pitted surface area fraction with coalescence $P(t,t_0)$ is divided by a number of equivalent pits per unit area $N_0^{eq}(P, t, t_0)$. This number of equivalent pits gives the same surface area and the same depth than a model which would take care of the volume coalescence of pits. N_0^{eq} is then smaller than N_0 in case of coalescence. But, as Model II neglects the intercepts between the volumes of the pits, the attacked volume is slightly underestimated. The surface area of an equivalent pit, A_p^{eq}, is easily calculated using:

$$A_p^{eq}(P, t, t_0) = \frac{P(t, t_0)}{N_0^{eq}(P, t, t_0)} \quad (24)$$

Knowing their shape and their depth, the mean volume of those equivalent pits, V_p^{eq}, can be expressed by:

$$V_p^{eq}(P, t, t_0) = A_p^{eq}(P, t, t_0) S_f k_d (t - t_0) = \frac{P(t, t_0)}{N_0^{eq}(P, t, t_0)} S_f k_d (t - t_0) \quad (25)$$

The total equivalent volume lost per unit area of the sample, $V_L^{eq_{tot}}/S$, is the sum of these volumes divided by the total area:

$$\frac{V_L^{eq_{tot}}}{S}(t, t_0) = N_0^{eq}(P, t, t_0) V_p^{eq}(P, t, t_0)$$
$$= N_0^{eq}(P, t, t_0) \frac{P(t, t_0)}{N_0^{eq}(P, t, t_0)} S_f k_d (t - t_0) = P(t, t_0) S_f k_d (t - t_0) \quad (26)$$

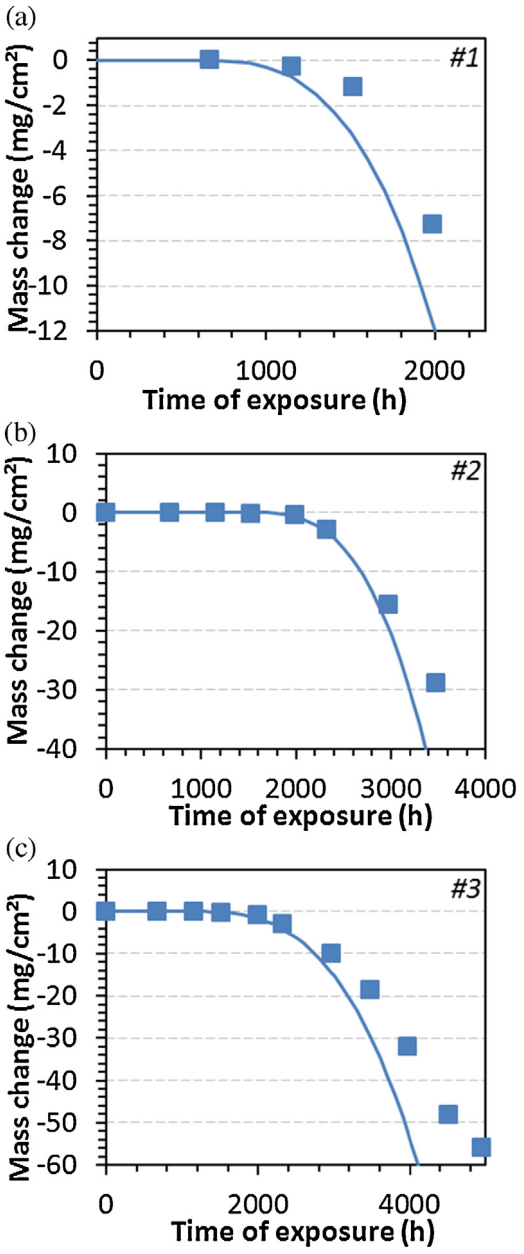

Fig. 13. Experimental net mass changes (squares) and mass losses modelled by Model I (continuous curve) for samples (a) #1, (b) #2 and (c) #3 in H_2–CO–CO_2–CH_4–H_2O at 570 °C, 21 bar.

Injecting Eq. (26) in Eq. (22), it is possible to express the resulting mass loss without considering explicitly the intercepts of the volumes of the pits:

$$\frac{\Delta m}{S}(t, t_0^{ext}, t_0^{int}) = -\rho_{all}\frac{V_L^{tot}}{S}(t, t_0^{ext}, t_0^{int})$$
$$= -\frac{1}{2}\rho_{all} S_f \left[P^{ext}(t, t_0^{ext}) k_d^{ext}(t - t_0^{ext}) + P^{int}(t, t_0^{int}) k_d^{int}(t - t_0^{int})\right] \quad (27)$$

The resulting mass loss increases slower than the one calculated with Model I as expected, because Model II takes into account surface coalescence. Despite it neglects volume coalescence, Model II describes with a good accuracy the experimental mass losses (Fig. 14). This shows that volume coalescence is

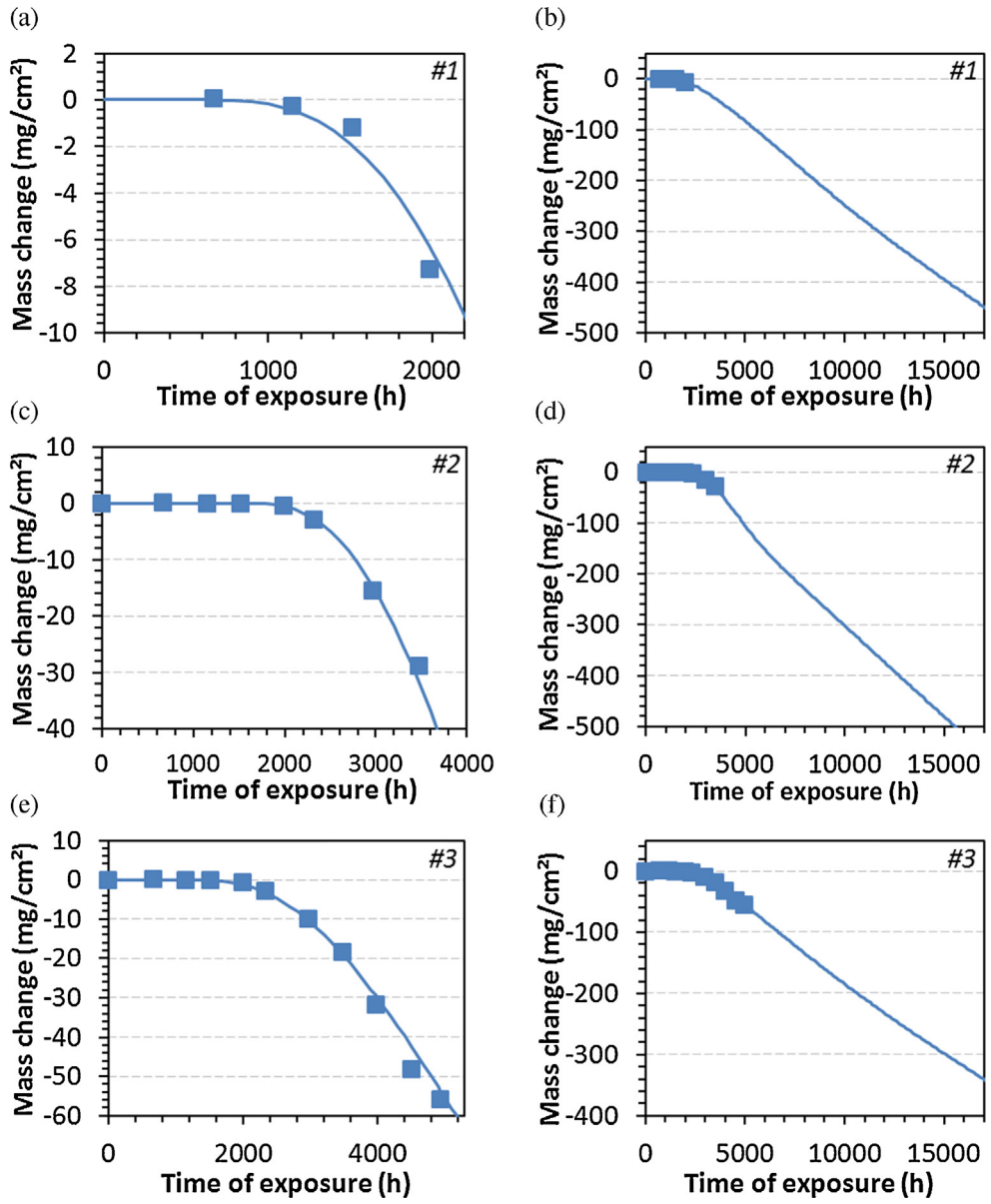

Fig. 14. Experimental net mass changes (squares) and mass losses modelled using Model II (curve) for samples (a and b) #1, (c and d) #2 and (e and f) #3 in H_2–CO–CO_2–CH_4–H_2O at 570 °C, 21 bar.

negligible for the pitted surface area fractions obtained in this study.

4.3.3. Model III: surface coalescence of pits with a right cylinder morphology

As can be seen on the cross section Fig. 8b, the shape of the merged pits is not spherical when coalescence occurs. Indeed, when coalescence between pits happens, the bottom of the pits flattens. The resulting shape of merged pits can be approximated by right cylinder morphology. Cylinder morphology is independent of the pit shape at the surface and is characterised by V_R equal to 1, then a S_f value equal to F (Model III in Fig. 12).

For an entirely attacked area, the resulting shape of the pits is then a right cylinder. Considering this shape for all pits from the beginning, the total volume lost (i.e. the volume of the pits) per unit surface area of the sample is calculated using the pitted area fraction obtained via Eq. (10). The mass loss is then expressed as:

$$\frac{V_L^{\text{tot}}}{S}(t,t_0)=\frac{1}{2}S_f\left[P^{\text{ext}}(t,t_0^{\text{ext}})k_{\text{d}}^{\text{ext}}(t-t_0^{\text{ext}})+P^{\text{int}}(t,t_0^{\text{int}})k_{\text{d}}^{\text{int}}(t-t_0^{\text{int}})\right] \quad (28)$$

The mass loss of the specimen can then be expressed by injecting Eq. (28) in Eq. (22):

$$\frac{\Delta m}{S}(t,t_0^{\text{ext}},t_0^{\text{int}})=-\rho_{\text{all}}\frac{V_L^{\text{tot}}(t,t_0^{\text{ext}},t_0^{\text{int}})}{S}$$
$$=-\frac{1}{2}\rho_{\text{all}}S_f\left[P^{\text{ext}}(t,t_0^{\text{ext}})k_{\text{d}}^{\text{ext}}(t-t_0^{\text{ext}})+P^{\text{int}}(t,t_0^{\text{int}})k_{d}^{\text{int}}(t-t_0^{\text{int}})\right] \quad (29)$$

As expected, Fig. 15 shows that the mass loss calculated with this model is larger than the experimental one. This is due to the fact that the volume of a cylinder is larger than the volume of a spherical cap with the same diameter. The difference of volume between cylinders and actual pits is maximal for the short exposure times. For longer exposure times, when coalescence increases, the shape of the coalesced pits gets closer to a cylinder, and experimental data should get closer to model III, which constitutes the asymptotic behaviour of the pitting kinetics.

The interest of this model resides in its ability to describe the case of entirely pitted specimens, i.e. for long exposure durations.

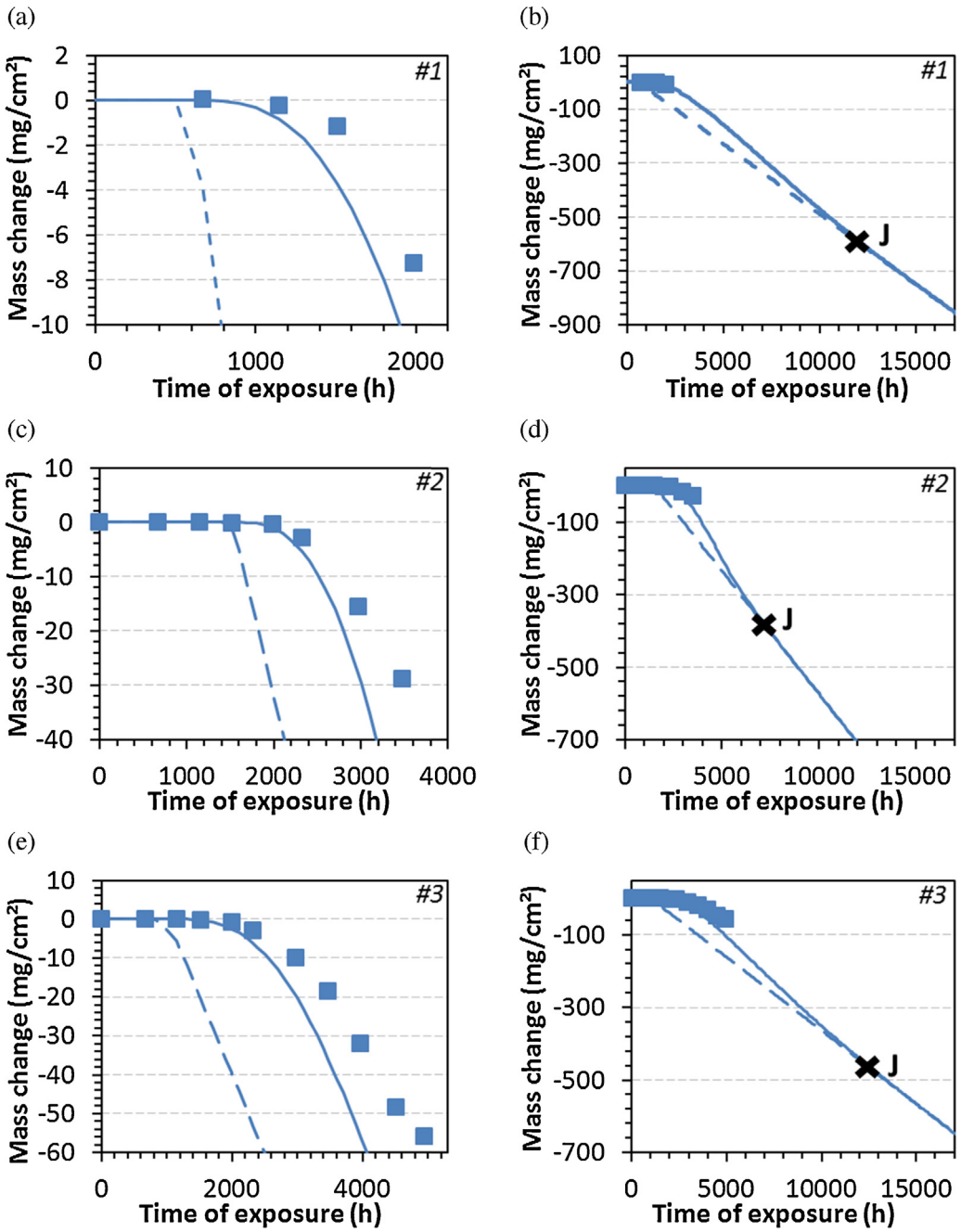

Fig. 15. Experimental net mass changes (squares) and mass losses modelled using Model III (continuous curve) and Model IV (dashed line) for samples (a and b) #1, (c and d) #2 and (e and f) #3 in H_2–CO–CO_2–CH_4–H_2O at 570 °C, 21 bar.

It maximises the attack and should then be used for conservative lifetime evaluation.

4.3.4. Model IV: conservative model for pits exhibiting a cylindrical morphology

It can be useful to anticipate the worst case scenario for the studied system, i.e. when the material cannot form a protective oxide scale. This worst case scenario can be described by expressing the pitted surface area fraction of both sample sides as a unit step function:

$$P^{\text{ext}}(t, t_0^{\text{ext}}) = \begin{cases} 0 \text{ for } t < t_0^{\text{ext}} \\ 1 \text{ for } t > t_0^{\text{ext}} \end{cases} \quad \text{and} \quad P^{\text{int}}(t, t_0^{\text{int}}) = \begin{cases} 0 \text{ for } t < t_0^{\text{int}} \\ 1 \text{ for } t > t_0^{\text{int}} \end{cases} \tag{30}$$

The mass loss can then be expressed by applying Eq. (30) in Eq. (29):

$$\frac{\Delta m}{S}(t, t_0^{\text{ext}}, t_0^{\text{int}}) = \begin{cases} -\frac{1}{2}\rho_{\text{all}} S_f \left[P^{\min(t_0^{\text{ext}}, t_0^{\text{int}})}\left(t, t_0^{\min(t_0^{\text{ext}}, t_0^{\text{int}})}\right) k_d^{\min(t_0^{\text{ext}}, t_0^{\text{int}})}\left(t - t_0^{\min(t_0^{\text{ext}}, t_0^{\text{int}})}\right)\right] & \text{for } \min(t_0^{\text{ext}}, t_0^{\text{int}}) < t < \max(t_0^{\text{ext}}, t_0^{\text{int}}) \\ -\frac{1}{2}\rho_{\text{all}} S_f \left[P^{\text{ext}}(t, t_0^{\text{ext}}) k_{\text{d}}^{\text{ext}}(t - t_0^{\text{ext}}) + P^{\text{int}}(t, t_0^{\text{int}}) k_{\text{d}}^{\text{int}}(t - t_0^{\text{int}}) \right] & \text{for } t > \max(t_0^{\text{ext}}, t_0^{\text{int}}) \end{cases} \tag{31}$$

According to Fig. 15, the mass loss calculated from Model IV decreases much faster than experimental data for short time exposures. Even if these calculated values are far from our experimental data, the experimental curves should reach this limit once the surface is entirely attacked. As expected, Model III reaches this conservative limit for long exposure times. The junction between these two models represents the time needed to obtain a pitted surface area fraction equal to 100% (Point J in Fig. 15).

5. Discussion

5.1. Pitting characteristics

It has been shown that pitting was characterised by an initial nucleation of pits after an incubation period t_0 (Fig. 5). The resulting pit density N_0 is not time dependent. Nishiyama et al. [21] observed a similar behaviour in a $60CO–26H_2–11.5CO_2–2.5H_2O$ environment at 1 bar and 650 °C, as Natesan and Zeng [22] in a $18.4CO–53.4H_2–5.7CO_2–22.5H_2O$ gas mixture at 14.3 bar and 593 °C (with $a_c = 31$ and $P_{O2} = 8.10^{-27}$ bar, close to our values). In the present study, pits are found to be circular and their lateral growth is characterised by a linear kinetics (Fig. 6) after the incubation time. A similar behaviour can be seen in the graphs previously published by Natesan and Zeng [22,34]. Nevertheless, in [22], the lateral growth rate of the pits eventually decreases and this was not explained. Nishiyama et al. [21] measured also the evolution of the pit diameter. Although they applied a parabolic law, the calculation deviated from experimental data and it is not sure if a linear law may have fitted better their data. To follow degradation by pitting, pit depth and pit geometry are of main interest. In this study, pits have a spherical-cap shape, with a constant pit depth/diameter ratio of about 0.2. This value is equal to the one measured by Natesan and Zeng [22] on the Ni-based alloys which suffered from the largest degradation after 9700 h of exposure (601, 602CA, 617, 45TM alloys).

5.2. Modelling

The main hypothesis for the modelling of the kinetics of pitting at the surface is the random pit distribution, which was not confirmed experimentally at first sight (Fig. 1). However, the ability of this modelling to reproduce the observed kinetics allows concluding that the attack kinetics is consistent with a random pit distribution on a given proportion of the surface, called the "reactive area". This "reactive area" represents 85% of the studied area for samples #1 and #3, 100% for sample #2, once the surface close to the edges of the sample has been removed from the analysis. Applying this model to the experimental pitted surface area allows to deduce the kinetics of pitting. The easiest way to apply the model is to measure the number of pits per unit area N_0. It is then possible to deduce the lateral pit growth rate constant k_d and the incubation time t_0 by fitting the pitted surface area $P(t,t_0)$ on the experimental data.

It was shown that several simple models can be used to reproduce and to extrapolate the kinetics of mass loss. In industrial applications, pitting occurs on large tubes, therefore these models which neglect the edge effects can be applied. A very simple conservative model (Model IV) was proposed for life modelling. But to go further with a more accurate descriptive model, it would be necessary to combine a model starting with spherical-cap pits (Eq. (27)) but taking into account volume coalescence via an increase in the constant S_f (Eq. (15)) until the entire surface is pitted – i.e. a V_R value of 1 and a S_f value of F.

6. Conclusion

800HT samples were attacked by metal dusting in a $H_2–CO–CO_2–CH_4–H_2O$ gas mixture at 21 bars. Sample surfaces experienced pitting leading to large mass losses. The kinetics of pitting was studied using image analysis. The pitting kinetics was characterised by an incubation time t_0 followed by the nucleation of a number of circular pits N_0. The number of pits did not increase during further exposure. Pits were circular and grew with a constant lateral growth rate, k_d. Pits showed a spherical cap morphology with a constant pit depth/diameter ratio, as already observed in the literature [22]. Yet, further work is necessary to determine the key parameters controlling pit nucleation and growth.

A simple nucleation-growth model has been developed using t_0, N_0 and k_d. The model reproduced very well the kinetics of metal dusting surface attack by pitting without the necessity to follow the growth of an important number of pits during thousands of hours. Indeed, the number of pits can be easily measured, as well as the total surface area which is attacked. Then, the incubation time t_0 could be considered as a shift parameter and the constant k_d the fit parameter. This model also showed that the pits are randomly dispersed on a large part of the surface (85–100%) which is sensitive to corrosion, whereas the remaining surface seems immune to the attack for the considered duration of exposure.

The constant pit depth/diameter ratio was used to extend the surface analysis to the volume. Therefore, the sample mass loss could be calculated from the surface pitting kinetics. Two types of models were developed in this study. The first one considered surface coalescence of pits but did not consider the volume coalescence. The second one considered the shape of the pits for an entirely attacked area – i.e. the pits are considered as right cylinders. It was observed that the spherical-cap morphology described with a good accuracy the experimental data, whereas the cylinder morphology is intended to describe experimental data for long exposures, when coalescence is important. The cylinder morphology model is therefore useful to build a safe conservative lifetime model.

The main strength of the present models resides in the limited information required to predict material degradation: pit number, incubation time, pit shape and lateral pit growth constant, mostly obtained via a surface analysis. This modelling is suitable to be applied to the internal attack of industrial tubes.

Acknowledgements

This work has been supported by the French National Research Agency through the project ANR SCAPAC 11-RNMP-0016 in partnership between Air Liquide, Veolia VERI, Sedis, University of Lorraine, CIRIMAT Laboratory.

Appendix.

Definition of the symbols used in this study

Symbol	Explanation
t	time (s)
t_0	incubation time (s)
k_d	lateral pit growth rate constant (m/s)
p	pit depth (m)
d	pit diameter (m)
F	p/d ratio for a pit
V	volume fraction of transformed phase
V_e	volume of transformed phase considering no overlap
$N_V(t,t_0)$	number of nuclei per unit volume (#/m^3)
$V_N(t,t_0)$	volume of a nucleus (m^3)
x	thickness axis (m)
θ	surface area fraction of transformed phase
$N(t,t_0)$	number of nuclei per unit area (#/m^2)
A	surface area of a nucleus (m^2)
N_p	pit number per unit area (#/m^2)
A_p	pit surface area (m^2)
P	pitted surface area fraction

B	parameter of Eq. (10)
V_p	pit volume (m^3)
S_f	shape factor defined in Eq. (14)
V_R	pit volume/cylinder volume ratio, Eq. (15)
$A_{p_i}(t, t_0)$	surface area of a given pit at time t
V_L	lost volume (m^3)
V_L^{tot}	total lost volume for a given sample (m^3)
ρ_{alloy}	alloy density (kg/m^3)
N_0^{eq}	equivalent number of pits per unit area ($\#/m^2$)
A_p^{eq}	equivalent pit surface area (m^2)
V_P^{eq}	equivalent pit volume (m^3)
S	sample surface area (m^2)

References

[1] R.F. Hochman, Metal deterioration in carbon monoxide and hydrocarbons at elevated temperatures, in: Third International Congress on Metallic Corrosion, University of Moscow Press, Moscow, USSR, 1966.
[2] R.F. Hochman, Catastrophic deterioration of high-temperature alloys in carbonaceous atmospheres, in: Symposium on Properties of High Temperature Alloys with Emphasis on Environmental Effects, Las Vegas, Nevada, 1976, pp. 715–732.
[3] H.J. Grabke, R. Krajak, J.C.N. Paz, On the mechanism of catastrophic carburization – metal dusting, Corros. Sci. 35 (1993) 1141–1150.
[4] H.J. Grabke, Thermodynamics, mechanisms and kinetics of metal dusting, Mater. Corros. 49 (1998) 303–308.
[5] H.J. Grabke, R. Krajak, E.M. Müller-Lorenz, S. StrauB., Metal dusting of nickel-base alloys, Mater. Corros. 47 (1996) 495–504.
[6] Z. Zeng, K. Natesan, V.A. Maroni, Investigation of metal-dusting mechanism in Fe-base alloys using Raman spectroscopy, X-ray diffraction, and electron microscopy, Oxid. Met. 58 (2002) 147–170.
[7] J.Q. Zhang, P. Munroe, D.J. Young, Microprocesses in nickel accompanying metal dusting, Acta Mater. 56 (2008) 68–77.
[8] H.J. Grabke, Metal dusting, Mater. Corros. 54 (2003) 736–746.
[9] D.J. Young, J. Zhang, C. Geers, M. Schütze, Recent advances in understanding metal dusting: a review, Mater. Corros. 62 (2011) 7–28.
[10] D. Monceau, E.M. Müller-Lorenz, H.J. Grabke, Metal dusting of stainless steels, Mater. Sci. Forum 251-254 (1997) 665–670.
[11] H.J. Grabke, E.M. Müller-Lorenz, B. Eltester, M. Lucas, D. Monceau, Resistance of 9–20%Cr-steels against metal dusting, Steel Res. 68 (1997) 179–185.
[12] S. Strauß, H.J. Grabke, Role of alloying elements in steels on metal dusting, Mater. Corros. 49 (1998) 321–327.
[13] J. Klöwer, H.J. Grabke, E.M. Müller-Lorenz, Metal dusting of nickel-base alloys, Mater. Corros. 49 (1998) 328–329.
[14] E.M. Müller-Lorenz, H.J. Grabke, Coking by metal dusting of steels, Mater. Corros. 50 (1999) 614–621.
[15] H.J. Grabke, C.B. Bracho-Troconis, E.M. Müller-Lorenz, Metal dusting of low alloy steels, Mater. Corros. 45 (1994) 215–221.
[16] R. Schneider, E. Pippel, J. Woltersdorf, S. Strauss, H.J. Grabke, Microprocesses of metal dusting on nickel and Ni-base alloys, Steel Res. 68 (1997) 326–332.
[17] M. Maier, J.F. Norton, P.D. Frampton, Metal dusting of 9–20% Cr steels in increased pressure environments at 560 °C, Mater. Corros. 49 (1998) 330–335.
[18] T.P. Levi, N. Briggs, I.E. Minchington, C.W. Thomas, Metal dusting of type 316 stainless steel in high pressure environments between 450 °C and 650 °C, Mater. Corros. 53 (2002) 239–246.
[19] D. Röhnert, F. Phillipp, H. Reuther, T. Weber, E. Wessel, M. Schütze, Initial stages in the metal-dusting process on alloy 800, Oxid. Met. 68 (2007) 271–293.
[20] B.A. Baker, G.D. Smith, V.W. Hartmann, L.E. Shoemaker, Nickel-base material solutions to metal dusting problems, in: Nace International Conference, Denver, 2002.
[21] Y. Nishiyama, N. Otsuka, T. Kudo, Metal dusting behaviour of Cr–Ni steels and Ni-base alloys in a simulated syngas mixture, Corros. Sci. 48 (2006) 2064–2083.
[22] K. Natesan, Z. Zeng, Development of Materials Resistant to Metal Dusting Degradation, report ANL-07/30, Argonne National Laboratory, 2007, pp. 161.
[23] C.-H. Chang, W.-T. Tsai, Carburization behavior under the pits induced by metal dusting in 304L and 347 stainless steels, Mater. Chem. Phys. 116 (2009) 426–432.
[24] B. Malki, B. Baroux, Computer simulation of the corrosion pit growth, Corros. Sci. 47 (2005) 171–182.
[25] D.J. Young, High Temperature Oxidation and Corrosion of Metals, Elsevier Corrosion Series, Amsterdam, 2008, pp. 592.
[26] A.N. Kolmogorov, A statistical theory for the recrystallization of metals, Bull. Acad. Sci. URSS (Cl. Sci. Math. Nat.) 3 (1937) 355.
[27] M. Avrami, Kinetics of phase change. I. General theory, J. Chem. Phys. 7 (1939) 1103–1112.
[28] M. Avrami, Kinetics of Phase Change. II. Transformation–time relations for random distribution of nuclei, J. Chem. Phys. 8 (1940) 212–224.
[29] M. Avrami, Granulation, Phase change, and microstructure kinetics of phase change. III, J. Chem. Phys. 9 (1941) 177–184.
[30] W.A. Johnson, R.F. Mehl, Reaction kinetics in processes of nucleation and growth, AIME Trans. (1939) 416–442.
[31] K.L. Mampel, Time–conversion formulae for heterogenous reactions in phase limits of solid bodies. 2. The time–conversion formulae for a powder from globular particles, Z. Phys. Chem. 187 (1940) 235–249.
[32] U.R. Evans, The laws of expanding circles and spheres in relation to the lateral growth of surface films and the grain-size of metals, Trans. Faraday Soc. 41 (1945) 365–374.
[33] T. Gheno, D. Monceau, D.J. Young, Kinetics of breakaway oxidation of Fe–Cr and Fe–Cr–Ni alloys in dry and wet carbon dioxide, Corros. Sci. 77 (2013) 246–256.
[34] Z. Zeng, K. Natesan, Control of metal dusting corrosion in Ni-based alloys, Int. J. Hydrog. Energy 32 (2007) 3640–3647.